

RADIO EMISSION SIGNATURES IN THE CRAB PULSAR

T. H. Hankins¹

J. A. Eilek¹

thankins@aoc.nrao.edu

jeilek@aoc.nrao.edu

ABSTRACT

Our high time resolution observations of individual pulses from the Crab pulsar show that both the time and frequency signatures of the interpulse are distinctly different from those of the main pulse. Main pulses can occasionally be resolved into short-lived, relatively narrow-band nanoshots. We believe these nanoshots are produced by soliton collapse in strong plasma turbulence. Interpulses at centimeter wavelengths are very different. Their dynamic spectrum contains regular, microsecond-long emission bands. We have detected these bands, proportionately spaced in frequency, from 4.5 to 10.5 GHz. The bands cannot easily be explained by any current theory of pulsar radio emission; we speculate on possible new models.

Subject headings: pulsars: individual (Crab Nebula pulsar) — radiation mechanisms: non-thermal

1. INTRODUCTION

What is the pulsar radio emission mechanism? Does the same mechanism always operate, in all stars or throughout the magnetosphere of one star? What are the physical conditions in the magnetosphere that allow the emission to happen? Despite forty years of effort, these questions still have not been answered conclusively.

Most models of pulsar radio emission fall into three groups. These are (1) antenna-type emission from coherent charge bunches; (2) strong plasma turbulence (SPT), in which non-linear effects convert plasma waves to electromagnetic waves which can escape the plasma;

¹Physics Department, New Mexico Tech, Socorro, NM 87801

and (3) several variants of maser emission. In Hankins *et al.* (2003; “HKWE”) we suggested these different emission mechanisms can be differentiated by their time signatures, because the characteristic variability timescales of each model differ. To test this idea, we designed and developed data acquisition systems to probe the radio emission signatures at the highest possible time resolutions. At low radio frequencies scattering by electron density inhomogeneities in the Crab Nebula and the interstellar medium mask the highest time and frequency resolution structure of the pulsar emission. The observations we describe here were made at high enough frequencies to avoid the pulse broadening, due to multipath propagation through the interstellar medium, which occurs at lower frequencies.

1.1. The Crab Pulsar

We have focused on the Crab pulsar because its occasional very strong “giant” pulses are ideally suited to our data acquisition systems. The mean profile of this star is dominated by a Main Pulse (MP) and an Interpulse (IP), as shown in Figure 1. Although the relative amplitudes and detailed profiles of these features change with frequency, they can be identified from low radio frequencies ($\lesssim 300$ MHz) up to the optical and hard X-ray bands. The similarity of the mean profile across this broad frequency range suggests that the radio emission and high-energy emission arise from the same regions of the magnetosphere in this star.

Several geometrical models have been proposed for the origin of the MP and IP emission in pulsars. Traditional radio-pulsar models ascribe MP/IP pairs to low-altitude emission (a few to a few tens of stellar radii) from highly relativistic outflows above the star’s two magnetic poles. Some models of high-energy pulsed emission also locate the emission regions at low altitudes (*e.g.*, Daugherty & Harding 1996). If this is the case, the magnetic axis of the Crab pulsar must be nearly orthogonal to its rotation axis in order to see the highly beamed emission from both poles. Alternatively, some authors have suggested that the magnetic and rotation axes are nearly aligned, and the MP and IP emission comes from a wide emission cone (*e.g.*, Manchester and Lyne 1977). Still other models relax constraints on the angle between the rotation and magnetic axes, and locate both radio and high-energy emission sites in the outer magnetosphere, possibly at the outer gap described by Cheng and Ruderman (1977). Yet another variant is the caustic model of Dyks *et al.* (2004), in which emission extends over a wide range of altitudes, from the star’s surface nearly to the light cylinder. (The Dyks *et al.* model suggests IP emission comes from higher altitudes than MP emission, as does one of the models discussed by Hankins and Cordes 1981).

We do not know which, if any, of these models are correct, but most of them suggest

physical conditions in the two emission regions should be similar. One would expect the same radio emission mechanism to be active in the IP and the MP. We were quite surprised, therefore, to find that the IP and MP have very different properties at high radio frequencies (5-10 GHz), as we report in this paper.

1.2. Observations and Post-processing

In 2002 we captured strong, individual Crab pulses at the Arecibo Observatory¹ at 2-ns time resolution, from 1.4–5 GHz, as reported in HKWE. For our new observations, reported here, we went to higher frequencies, 6–8.5 GHz and 8–10.5 GHz, in order to obtain 2.5-GHz bandwidth and consequent 0.4-ns time resolution. For pulses that exceeded a preset threshold the received voltages from both polarizations were digitized with 8-bit resolution and stored for off-line coherent dedispersion. This allowed us to reach intrinsic time resolutions down to the limit imposed by the inverse of the receiver bandwidth, 0.4 ns. In §2 and §3 we show dedispersed individual pulses and their dynamic spectra² recorded at 8-10.5 GHz for all of our figures; the results at 6-8.5 GHz are similar in all characteristics.

After capturing a pulse our data acquisition system requires more than a pulse period to store the data and be reset to capture another pulse. Therefore we record only pulses which exceed a preset threshold, which we set high enough to trigger the data acquisition system only for the brightest individual pulses. The trigger detector bandwidth was typically 0.5 GHz, centered on the 2.5-GHz sampled bandwidth.

The pulses we record coincide with the high-flux power law tail of the number-*vs.*-flux histogram for single pulses, as seen by Argyle and Gower (1972) and Lundgren *et al.* (1995) at lower frequencies; thus they might be loosely called “giant” pulses. However, it is not yet clear whether these high-flux pulses are physically similar to, or different from, the more common “weak” pulses; we are not aware of any compelling evidence for either case. In what follows we do not attempt to distinguish between the two, but just discuss MPs or IPs.

At the high time resolution we achieve, details of the pulses are sensitive to the exact value of the dispersion measure (DM) used for the coherent dedispersion operation. We generally started with the DM value given by the Jodrell Bank Crab Pulsar Monthly

¹The Arecibo Observatory is part of the National Astronomy and Ionosphere Center, which is operated by Cornell University under a cooperative agreement with the National Science Foundation.

²The dynamic spectrum is computed from the dedispersed voltage time series. It shows how the received pulse intensity is distributed in time and radio frequency.

Ephemeris³ for our observing epochs. However, we found evidence in the dynamic spectra that individual pulses could be more or less dispersed than the tabulated value, and that IPs are systematically more dispersed than MPs, as discussed in §3. We then attempted to find the “optimum” DM for most of the pulses we show in this paper. For a narrow pulse, such as most components of a MP, we used the DM value which maximized the peak intensity and the intensity variance, minimized the width, and aligned the arrival times of emission throughout our bandwidth. As shown in §3 and Figures 6, 7 and 8 the typical IPs are broader than the MPs; alignment of the dynamic spectra provided more reliable DM estimates for the IPs. We found it necessary to refine our optimum DM to a resolution of 10^{-5} pc-cm⁻³.

In the remainder of this paper we present our observations of the main pulse in §2, then the interpulse and its narrow emission bands in §3. In §4 we discuss some possible causes of the interpulse emission bands and model limitations, and summarize our results in §5.

2. THE MAIN PULSE

In our first high time resolution observations of the Crab pulsar (reported in HKWE), we concentrated on the MP, because it is brighter at low frequencies, and strong pulses are more common at the phase of the MP (Cordes *et al.* 2004). Our new observations at higher frequencies, 6-8.5 GHz and 8-10.5 GHz at Arecibo, confirm and extend our original results on the MP.

2.1. Microbursts and Nanoshots

Most MPs consist of one to several “microbursts”; the brightest microburst in an MP can occur anywhere within the pulse average envelope. The microbursts can often be resolved into overlapping, short-lived “nanoshots”. Figures 2 and 3 shows typical examples of MPs; other examples are shown in Sallmen *et al.* (1999) and Kern (2004).

The dynamic spectrum of the microbursts is broadband, filling our entire observing bandwidth. The emission is sometimes, but not always, slightly weaker toward the high frequency edge of the receiver band (as illustrated in Figures 2 and 3). This is unlikely to be due to instrumental or interstellar effects. We normalized our system gain, as a function of frequency, by the Crab Nebula background which dominates the off-pulse system

³www.jb.man.ac.uk/~pulsar/crab.html

temperature. The nebular spectrum is quite flat (proportional to $\nu^{-0.26}$ at these frequencies; Baars & Hartsuiker 1972). The correlation bandwidth due to interstellar scintillation (ISS) is predicted to be $\sim 1 - 2$ GHz at 8-10 GHz, and scales approximately as ν^4 (Cordes *et al.* 2004, Kern 2004). We might expect interstellar effects occasionally to be seen in the dynamic spectrum, but such effects should be equally likely to be seen at the lower edge of the passband, as at the high edge. We therefore conclude that the high-frequency fading sometimes seen in the dynamic spectrum of the MP is intrinsic to the MP emission mechanism. This is consistent with the known steep radio spectrum of the Crab pulsar ($\nu^{-3.1}$; Manchester, *et al.* 2005).

While most MPs resemble the examples in Figures 2 and 3, occasionally the nanoshots are sufficiently sparse to be seen individually. Figure 4 shows one example. When this is the case, some of the nanoshots turn out to be relatively narrow-band. We believe these new data support our argument, in HKWE, that each MP microburst is a collection of short-lived nanoshots. When the time resolution is high enough, and the nanoshots are well separated in time, the individual shots can be resolved. We note that this picture is consistent with previous modeling of pulsar emission as amplitude-modulated noise, produced by the ensemble of a large number of randomly occurring nanoshot pulses, modulated by a more slowly varying amplitude function (Rickett 1975).

2.2. Our Interpretation: Strong Plasma Turbulence

We argued in HKWE that the nanoshots represent the fundamental emission mechanism in MPs. In that paper we compared the nanoshots to predictions of the three competing theoretical models of the radio emission mechanism. We found that the short durations and narrow bandwidths of the nanoshots are consistent *only* with predictions of the SPT model. They are not consistent with predictions of scaling arguments describing emission from masers or from coherent charge bunches (both of which predict longer characteristic times). In particular, Weatherall (1998) modeled SPT and predicted narrow-band radiation, $\delta\nu/\nu \sim 0.1 - 0.2$, centered on the co-moving plasma frequency. He also predicted a distinctive time signature, arising from the coupling of the electromagnetic modes to the turbulence: $\nu\delta t \sim O(10)$. The relatively narrow-band spectra of the nanoshots revealed by our new observations match Weatherall’s models well. We thus confirm our suggestion, in HKWE, that coherent radio emission in MPs is plasma emission produced by collapsing solitons in strong plasma turbulence.

We note, however, that the SPT model makes no predictions on the spectrum of a collection of nanoshots. The spectral steepening we sometimes see in the MP dynamic

spectrum could be due either to fewer nanoshots within a high-frequency microburst, or to less energy released in a single high-frequency nanoshot, or both.

This model does make one important prediction: plasma flow in the radio emission region is likely to be unsteady. The plasma flow will be smooth only if the local charge density is exactly the Goldreich-Julian (1969; “GJ”) value, $\rho_{\text{GJ}} \simeq \Omega B / 2\pi c$ (for a rotation rate Ω), so that the rotation-induced electric field is fully shielded. If the charge density differs from ρ_{GJ} , the emitting plasma feels an unshielded electric field, and feeds back on that field as its charge density fluctuates, leading to unsteady plasma flow (and consequently unsteady radio emission).

For the Crab pulsar, making the usual assumption that its spindown is due to magnetic dipole radiation, we estimate a field $B(r) \simeq 4 \times 10^{12}$ G, and a GJ density $n_{\text{GJ}}(r) = \rho_{\text{GJ}}(r)/e \simeq 8 \times 10^{12} \text{ cm}^{-3}$, close to the star’s surface. At the light cylinder, $\sim 160r_*$, the field drops to $\sim 1 \times 10^6$ G and the GJ density to $\sim 2 \times 10^6 \text{ cm}^{-3}$. Current pair cascade models predict that the (neutral) pair density exceeds the primary beam (GJ) density by a factor $\lambda \sim 10^2 - 10^3$ (Arendt & Eilek 2002). Now, if SPT is the emission mechanism, we can determine the plasma density directly, because SPT emission is centered on the comoving plasma frequency ($\nu_p \propto \sqrt{\gamma_b n}$, for bulk Lorentz factor γ_b). Thus, emission at frequency ν comes from plasma density $n\gamma_b \simeq 1.2 \times 10^{10} \nu_{\text{GHz}}^2 \text{ cm}^{-3}$. Noting that current models predict $\gamma_b \sim 10^2 - 10^3$ (*e.g.*, Arendt & Eilek), and using λ to convert from plasma density to charge density, our SPT argument predicts that 1-GHz emission comes from a region with number density of excess charge $\sim 10^4 - 10^6 \text{ cm}^{-3}$, and 9.5-GHz emission comes from $\sim 10^6 - 10^8 \text{ cm}^{-3}$. The higher density values may be consistent with GJ conditions at moderate to high altitudes; the lower values are very unlikely to satisfy GJ conditions anywhere in the magnetosphere. We therefore suggest the highly unsteady, bursty MP emission we see from 1 to 10 GHz reflects unsteady plasma flow due to sub-GJ charge densities in the emission region (*cf.* also Kunzl *et al.* 1998, who drew the same conclusion from a somewhat different argument).

2.3. Extreme Nanoshots

The nanoshots can occasionally be extremely intense. In Figure 5 we show a single MP which exceeds 2 MJy, and has an unresolved duration of less than 0.4 ns. If we ignore relativistic effects (following, *e.g.*, Cordes *et al.* 2004), we estimate a light-travel size $c\delta t \simeq 12$ cm. From this we find an implied brightness temperature 2×10^{41} K, which we believe is the highest ever reported for pulsar emission. Alternatively, we might assume the emitting structure is moving outwards with Lorentz factor $\gamma_b \sim 10^2 - 10^3$. If this is the case, our size

estimate increases to $10^3 - 10^5$ cm, and the brightness temperature decreases to $10^{35} - 10^{37}$ K.

The extremity of this pulse can also be demonstrated in terms of local quantities. If the pulse is emitted from a structure moving at γ_b , its energy density is $u_{\text{rad}} \sim 4 \times 10^{23} / \gamma_b^4$ erg cm^{-3} . This high energy density can be compared to the plasma energy density, $u_{\text{pl}} = \gamma_b n m c^2$, which we can estimate either from our assumption of SPT emission (which gives a lower density), or by assuming that GJ conditions hold (which gives a higher density). In either case, we find $u_{\text{rad}} \gg u_{\text{pl}}$, unless γ_b is extremely large. As noted in HKWE, this emphasizes the need for a collective emission process. For another comparison, we can convert the energy density in the radiation pulse to an equivalent electric field, $E \sim 3.2 \times 10^{12} / \gamma_b^2$ G, giving a wave-strength parameter $eE / 2\pi m_e c \nu \gg 1$. It follows that magnetospheric propagation of such strong nanoshots will be complex and nonlinear (*e.g.*, Chian & Kennel 1983).

3. THE INTERPULSE

In order to test our hypothesis that strong plasma turbulence governs the emission physics in the Crab pulsar, we went to higher frequencies to get a larger bandwidth and shorter time resolution. In addition to the MP, we observed single pulses from the IP, because at high frequencies strong pulses are far more common at the rotation phase of the IP. When we observed IPs and MPs with a broad bandwidth, from 6-8 or 8-10.5 GHz, we were astonished to find that IPs have very different properties from MPs.

3.1. Characteristics

We recorded about 220 individual MPs, and about 150 individual IPs, between 4.5 and 10.5 GHz, during 20 observing days from 2004 to 2006. Together with our earlier results (Moffett & Hankins 1999), these data reveal that the high-frequency IP differs from the MP in intensity, time signature, polarization, dispersion and spectrum. In this subsection we discuss the first four properties; we defer discussion of the spectrum to the next subsection. We illustrate our discussion with Figures 6, 7 and 8 which show three typical IPs.

3.1.1. Intensity

Strong IPs are at least an order of magnitude more frequent than strong MPs at 9 GHz, but the MPs can be considerably stronger than the IPs when they occur. This can be seen in the examples shown in this paper, as well as in the the signal-to-noise-ratio histograms of

Figure 3 of Cordes *et al.* (2004) and the scatter plots of their Figure 5 (where the signal-to-noise-ratio of MPs and IPs are shown as a function of pulse phase).

3.1.2. Polarization

High-frequency IPs are more strongly polarized than MPs. Moffett & Hankins (1999) showed that the IP is strongly linearly polarized, 50-100% at 4.9 GHz, while the MP is only weakly polarized. We showed in HKWE that individual nanoshots in the MP can be strongly polarized, but the polarization changes dramatically from one nanoshot to the next. This leads to weak MP polarization when the nanoshot density is high or the pulse is smoothed to $\sim 1\mu\text{s}$.

3.1.3. Time signature

IP emission is not broken up into the short-lived microbursts that characterize the MP. Instead, it is more continuous in time, spread out over a few microseconds. When optimally dedispersed, IPs usually have a very rapid onset, followed by a slower decay and often similar secondary bursts. To quantify the time duration of the IPs, we used the equivalent width of the intensity autocorrelation function to estimate the IP duration. In Figure 9 we show the distribution of equivalent widths for all of the IPs we recorded at and above 6 GHz. This figure shows that IPs typically last several microseconds at 6-8 GHz, and become shorter at higher frequencies.

Because the temporal behavior of MPs is much more complex (as we discussed in §2; *cf.* Figures 2 and 3), the question “what is the characteristic time signature of an individual MP” is difficult to answer. We discuss MP time scales in a forthcoming paper.

3.1.4. Dispersion

IPs are more dispersed than MPs measured at the same time. As an example, the IP in Figure 6 was observed 12 minutes after the MP shown in Figure 2, and processed identically. The dynamic spectrum of the IP shows that lower frequencies arrive later than high frequencies; we take this as evidence for extra dispersion in the IP. Because we consistently found IPs more dispersed than MPs observed on the same day, we conclude this extra dispersion must occur *in the pulsar’s magnetosphere*.

It is hard to compare the data to predictions of magnetospheric dispersion, because we do not know the correct dispersion relation for the magnetospheric plasma. As a simple example, consider dispersion from a cold, unmagnetized plasma. The $0.65\text{-}\mu\text{s}$ delay between 8.4 and 10.4 GHz, for the pulse shown in Figure 6, would correspond to an excess dispersion measure, $\sim 0.032\text{ pc-cm}^{-3}$ ($\sim 10^{-3}$ of the total DM measured by Jodrell Bank). If the magnetosphere were filled with cold plasma at the GJ density, it would have a column density $\sim 1.3\text{ pc-cm}^{-3}$, far more than enough to account for the excess DM of the IP. But this estimate is naive. Most of the magnetosphere is strongly magnetized, and at low altitudes charges are constrained to move only along field lines. A more realistic dispersion law is needed, but without knowing conditions through which the pulse propagates it is not clear which law to choose.

We discuss these complex issues more fully in a separate paper (Crossley *et al.* 2007).

3.2. Emission Bands

The most striking difference between the interpulse and the main pulse is found in the dynamic spectrum. An IP contains microsecond-long trains of *emission bands*, as illustrated in Figures 6, 7 and 8. *Every* IP we have recorded displays these emission bands. However, MPs recorded during the same observing sessions and processed identically do not show the bands. The bands are, therefore, not due to instrumental or interstellar effects, but are intrinsic to the star.

3.2.1. Properties of the Emission Bands

The emission bands are grouped into regular “sets”; 2 or 3 band sets, regularly spaced, can usually be identified in a given IP. Individual band sets last no more than a few microseconds. All bands in a particular set appear almost simultaneously, certainly to within $\Delta t_{\text{start}} < 100\text{ ns}$ for optimally dedispersed pulses. This requires that all of the bands must originate from a region no more than $d = c\Delta t_{\text{start}} < 30\text{ m}$ in size.

The IPs show a sharp onset, which is often associated with a very short-lived ($\leq 100\text{ ns}$) band set. Additional band sets often turn on part way through the pulse, producing secondary bursts of total intensity which also show the characteristic fast-rise-slow-decay time signature. Band sets that begin later tend to last longer, up to the few-microsecond duration of the total pulse.

At first glance the bands appear to be uniformly spaced. However, closer inspection of

our data shows that the bands are *proportionally spaced*. Figure 10 shows that the spacing between two adjacent bands depends on the mean frequency, as $\Delta\nu/\nu \simeq 0.06$. Thus, two bands near 6 GHz are spaced by ~ 360 MHz; two bands near 10 GHz are spaced by ~ 600 MHz. This proportional spacing is robust; a set of emission bands can drift in frequency (usually upwards, as in Figures 6, 7 and 8), but their frequency spacing stays constant. We note that the least-squares fitted line in Figure 10 is consistent with zero spacing at zero frequency; however we do not think that the bands continue to very low frequencies (as we discuss in the next section).

The frequency profile of a given band tends to be peaked about a central frequency, *i.e.* closer to Gaussian than to rectangular or impulsive. The frequency width of an emission band, estimated by eye as a half power width, is typically 10-20% of the spacing between bands. Within a single IP the center frequency of an emission band often remains steady until the band disappears. In some instances, however, the center frequency drifts upwards during the band duration, by no more than 20-30% of the band spacing. We have occasionally seen bands that appear to drift slightly downward in frequency, but this is rare. Bands sets that begin later in the pulse tend to start at frequencies slightly higher than the early bands, but againw the frequency shift is less than the spacing between bands. These features are all illustrated in Figures 6, 7 and 8. We note that quantitative analysis of the structure of a single band is limited by the frequency resolution we can achieve for short-lived bands, by signal-to-noise limits and the overlap of separate band sets.

3.2.2. Frequency Extent of the Bands

We suspect the bands extend over at least a 5-6 GHz bandwidth in a single IP, but do not occur below ~ 4 GHz. While we have not been able to observe more than 2.2 GHz simultaneously, we have seen no evidence that a given band set cuts off within our observable bandwidth. The characteristics of the bands (proportional spacing, duration, onset relative to total intensity microbursts) are unchanged from 5 to 10 GHz.

We have captured a few IPs between 4 and 5 GHz, but the bands are unclear in all of them. We suspect the dynamic spectrum in this frequency range has been corrupted by ISS, for which the correlation bandwidth is predicted to be ~ 100 MHz at these frequencies, somewhat less than the band spacing projected from Figure 10. Technical limitations, involving terrestrial radio interference and the high-speed memory capacity of our data acquisition system, kept us from observing with enough bandwidth to investigate the existence of bands below ~ 4 GHz. We note, however, that mean profiles suggest the nature of the IP changes between 1 and 4 GHz. From Figure 1 (also Cordes *et al.* 2004) we see that the

IP between 4 and 8 GHz appears at an earlier phase than at ≤ 1.4 GHz, and there is no IP at all around 3 GHz. This leads us to believe that the low and high radio frequency IPs are unrelated; we therefore expect no IP band emission below 4 GHz.

Unlike the MPs, there is no indication in our data that the band intensity is weaker at high frequencies. From this we infer that the IP spectrum is flatter than the MP spectrum. The IP spectrum may, in fact, be atypical of radio emission from the general pulsar population, which is known to be steep spectrum.

We reiterate that the emission bands in the IP cannot be due to ISS. Their clear regularity, the fact that they exist only in the IP and not in MPs observed at the same time, and their $\Delta\nu \propto \nu$ spacing, all disagree with known properties of ISS, and point to an origin intrinsic to the IP.

4. POSSIBLE CAUSES OF THE EMISSION BANDS

The dynamic spectrum of the interulses does not match any of the three types of emission models described in §1. Because each of the models predicts narrow-band emission at the plasma frequency, *none of them can explain the dynamic spectrum of the IP*. A new approach is required here, which may “push the envelope” of pulsar radio emission models.

While we remain perplexed by the dramatic dynamic spectrum of the interpulse, we have explored possible models. This exercise is made particularly difficult by the fact that the emission bands are not regularly spaced. Because of this, models that initially seemed attractive must be rejected. As an example, if the emission bands were uniformly spaced they could be the spectral representation of a regular emission pulse train. Many authors have invoked regularly spaced plasma structures (sparks or filaments), whose passage across the line of sight could create such a pulse train. Alternatively, strong plasma waves with a characteristic frequency will also create a regular emission pulse train. The dynamic spectrum of either of these models would contain emission bands at constant spacing; the *proportional* spacing we observe disproves both of these hypotheses.

We looked to solar physics for insight. We initially considered split bands in the dynamic spectra of Type II solar flares, which are thought to be plasma emission from low and high density regions associated with a shock propagating through the solar corona. This does not seem to be helpful for the Crab pulsar emission bands, because the radio-loud plasma would have to contain 10 or 15 different density stratifications, which seems unlikely. However, “zebra bands” seen in Type IV solar flares may be germane. These are parallel, drifting, narrow emission bands seen in the dynamic spectra of Type IV flares. Band sets

containing from a few up to ~ 30 bands have been reported, with fractional spacing $\Delta\nu/\nu \sim .01 - .03$ (*e.g.*, Chernov *et al.* 2005; Sawant *et al.* 2005). While zebra bands have not yet been satisfactorily explained, two classes of models have been proposed, namely resonant plasma emission and geometrical effects. It may be that these models will provide clues to understanding the emission bands in the Crab pulsar.

4.1. Resonant cyclotron emission

One possibility is plasma emission at the cyclotron resonance, $\omega - k_{\parallel}v_{\parallel} - s\Omega_0/\gamma = 0$ (where γ is the particle Lorentz factor, $\Omega_0 = eB/mc$, and s is the integer harmonic number). Kazbegi *et al.* (1991) proposed that this resonance operates at high altitudes in the pulsar magnetosphere, possibly generating both X-mode waves (which can escape the plasma directly) and O-mode waves; a related model is being applied to the Crab emission bands by Lyutikov (2007, private communication). Alternatively, double resonant cyclotron emission at the plasma resonant frequency has been proposed for zebra bands in solar flares (*e.g.*, Winglee & Dulk 1986). In solar conditions, this resonance generates O-mode waves, which must mode convert in order to escape the plasma. The emission frequency in these models is determined by local conditions where the resonance is satisfied; the band separation is $\Delta\nu \simeq \Omega_0/2\pi\gamma$. It is not clear how the specific, proportional band spacing can be explained in such models; perhaps a local gradient in the magnetic field can be invoked.

Such models face several additional challenges before they can be considered successful. The emission must occur at high altitudes, in order to bring the resonant (cyclotron) frequency down to the radio band. Close to the light cylinder, where $B \sim 10^6$ G, particle energies $\gamma \sim 500 - 1000$ could radiate at 5 - 10 GHz. In addition, such models must be developed by means of specific calculations which address the fundamental plasma modes and their stability, under conditions likely to exist at high altitudes in the pulsar's magnetosphere.

4.2. Geometrical models

Alternatively, the striking regularity of the bands calls to mind a special geometry. If some mechanism splits the emission beam coherently, so that it interferes with itself, the bands could be interference fringes. For instance, a downwards beam which reflects off a high density region could return and interfere with its upwards counterpart on the way back up (*e.g.*, Ledenev *et al.* 2001 for solar zebra bands). Simple geometry suggests that fringes

occur if the two paths differ in length by only $c/\Delta\nu \lesssim 1$ m. Another geometrical possibility is that cavities form in the plasma and trap some of the emitted radiation, imposing a discrete frequency structure on the escaping radiation (*e.g.*, LaBelle *et al.* 2003). The scales required here are also small; the cavity scale must be some multiple of the wavelength, *i.e.*, several centimeters.

Geometrical models need an underlying broad-band radiation source, with at least 5-GHz bandwidth, in order to produce the emission bands we observe. Because standard pulsar radio emission mechanisms lead to relatively narrow-band radiation, at the local plasma frequency, they seem unlikely to work here. A double layer might be the radiation source; charges accelerated within the layer should radiate broadband, up to $\nu \sim L/2\pi c$, if L is the thickness of the double layer (*e.g.*, Kuipers 1990; Volwerk 1993). This is also a small-scale effect; emission at 10 GHz requires $L \sim 1$ cm. This may be consistent with the thickness of a relativistic, lepton double layer, which we estimate as several times $c/2\pi\nu_p$ (following, *e.g.*, Carlqvist 1982).

Geometrical models also face several challenges before they can be considered successful. The basic geometry is a challenge: what long-lived plasma structures can lead to the necessary interference or wave trapping? Once again, it is not clear how the proportional band spacing can be explained; perhaps a variable index of refraction in the interference or trapping region can be invoked.

5. Summary and conclusions

We have observed individual pulses from the Crab pulsar with 2.2-GHz bandwidth and 0.4-ns time resolution. We observed both the main pulse (MP) and the interpulse (IP), at high radio frequencies (5–10 GHz). We were very surprised when our observations revealed that the MP and the IP are strikingly different. At these frequencies, MPs consist of many short-lived, relatively narrow-band, nanoshots. Both the time and frequency signatures of the nanoshots are consistent with predictions of one current model of pulsar radio emission, namely, coherent emission from strong plasma turbulence.

IPs, however, differ from MPs in their time, polarization, dispersion and spectral signatures. It seems that the MP and the IP differ in their emission mechanisms and their propagation within the magnetosphere. The dynamic spectrum of the IP contains regularly spaced emission bands, which do not match the predictions of any current model. Our result is especially surprising because magnetospheric models generally ascribe the MP and the IP to physically similar regions, which simply happen to be on opposite sides of the star. One

would therefore expect the MP and the IP to have similar characteristics, which is exactly *not* what we find.

The work of Moffett & Hankins (1996) may provide an important clue. They discovered new components in the mean profile at 5 and 8 GHz, which appear at offset rotation phases, and only at high radio frequencies. They also found that the IP at high radio frequencies appears at an earlier rotation phase than its counterpart at both lower (radio below 2 GHz) and higher (optical to X-ray) frequencies. It is just this high-radio-frequency IP which we discuss in this paper. We speculate that this IP, and the other high-radio-frequency components Moffett & Hankins found, originate in an unexpected part of the star’s magnetosphere, where different physical conditions produce quite different radiation signatures.

We appreciate helpful conversations with Joe Borovsky, Alice Harding, Axel Jessner, Jan Kuijpers, Maxim Lyutikov, and the members of the Socorro pulsar group. We thank our referee for constructive comments which improved the paper. We particularly thank our students, Jared Crossley, Eric Plum and James Sheckard for their help with observations. This work was partially supported by the National Science Foundation, through grants AST0139641 and AST0607492.

REFERENCES

- Arendt, P.N. Jr. & Eilek, J.A., 2002, ApJ, 581, 451
- Argyle, E., & Gower, J.F.R. 1972, ApJ, 175, L89
- Baars, J.W.M. & Hartsuijker, A.P., 1972, A&A, 17, 172
- Carlqvist, P., 1982, ApSS, 87, 21
- Cheng, A.F. & Ruderman, M.A., 1977, ApJ, 216, 865
- Chian, A.C.-L. & Kennel, C.F., 1982, Ap&SS, 97, 9
- Chernov, G.P., Yan, Y.H., Fu, Q.J. & Tah, Ch.M., 2005, A&A, 437, 1047
- Cordes, J.M., Bhat, N.D.R., Hankins, T.H., McLaughlin, M.A. & Kern, J., 2004, ApJ, 612, 375
- Crossley, J.M., Hankins, T.H. & Eilek, J.A., 2007, in preparation
- Daugherty, J.K. & Harding, A.K., 1996, ApJ, 300, 500

- Dyks, J., Harding, A.K. & Rudak, B., 2004, ApJ, 606, 1125
- Goldreich, P. & Julian, W.H., 1969, ApJ, 157, 869
- Goodman, J., & Narayan, R. 1985, MNRAS, 214, 519
- Hankins, T.H., & Cordes, J.M., 1981, ApJ, 249, 241
- Hankins, T.H., Kern, J.S., Weatherall, J.C. & Eilek, J.A., 2003, Nature, 422, 141
- Isaacman, R., & Rankin, J. M. 1977, ApJ, 214, 214
- Kazbegi, A.Z., Machabeli, G.Z. & Melikidze, G.I., 1991, MNRAS, 253, 377
- Kern, J., 2004, Ph.D. thesis, New Mexico Tech
- Kuijpers, J., 1990, in *Plasma Phenomena in the Solar Atmosphere*, eds. M. Dubois, F. Bely-Dubau & D. Gresillon (Editions de Physique, France), p. 17
- Kunzl, T., Lesch, H., Jessner, A. & von Hoensbroech, A., 1998, ApJ, 505, L139
- LaBelle, J., Treumann, R.A., Yoon, P.H. & Karlicky, M., 2003, ApJ, 593, 1195
- Ledenev, V.G., Karlický, M., Yan, & Fu, Q., 2001, Sol Phys., 202, 72
- Lundgren, S.C., Cordes, J.M., Ulmer, M., Matz, S.M., Lomatch, S., Foster, R.S., & Hankins, T. 1995, ApJ, 453, 433
- Manchester, R.N., Hobbs, G.B., Teoh, A., & Hobbs, M. 2005, AJ, 129, 1993
- Moffett, D.A. & Hankins, T.H., 1996, ApJ, 468, 779
- Manchester, R.N. & Lyne, A.G., 1977, MNRAS, 181, 761
- Moffett, D.A. & Hankins, T.H., 1999, ApJ, 522, 1046
- Rickett, B.J., 1975, ApJ, 197, 185
- Sallmen, S., Backer, D.C., Hankins, T.H., Moffett, D., & Lundgren, S. 1999, ApJ, 517, 460
- Sawant, H.S., Karlický, M., Fernandes, F.C.R. & Cecatto, J.R., 2002, AA, 396, 1015
- Volwerk, 1993, J Phys D, 26, 1192
- Weatherall, J.C., 1998, ApJ, 506, 341
- Winglee, R.M. & Dulk, G.A., 1986, ApJ, 307, 808

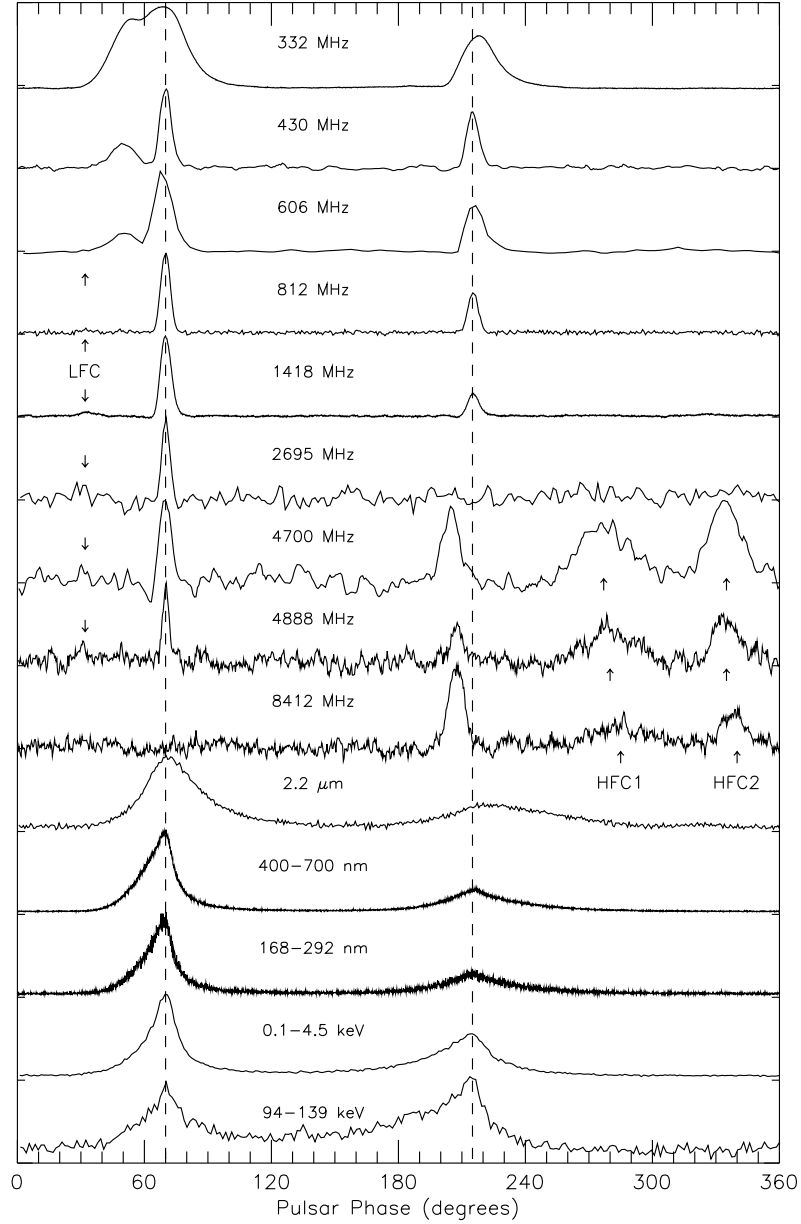


Fig. 1.— The mean profile of the Crab pulsar, over a wide range of frequencies (from Moffett & Hankins 1996). The main pulse and interpulse, shown by dashed lines at pulse phases 70° and 215° , persist from radio to hard X-ray bands. However, between 4.7 and 8.4 GHz the interpulse is offset from the interpulse at lower and higher frequencies, and new components appear (labeled HFC1 and HFC2). These intermediate-frequency components may have a different origin from the lower and higher frequency interpulse and main pulse.

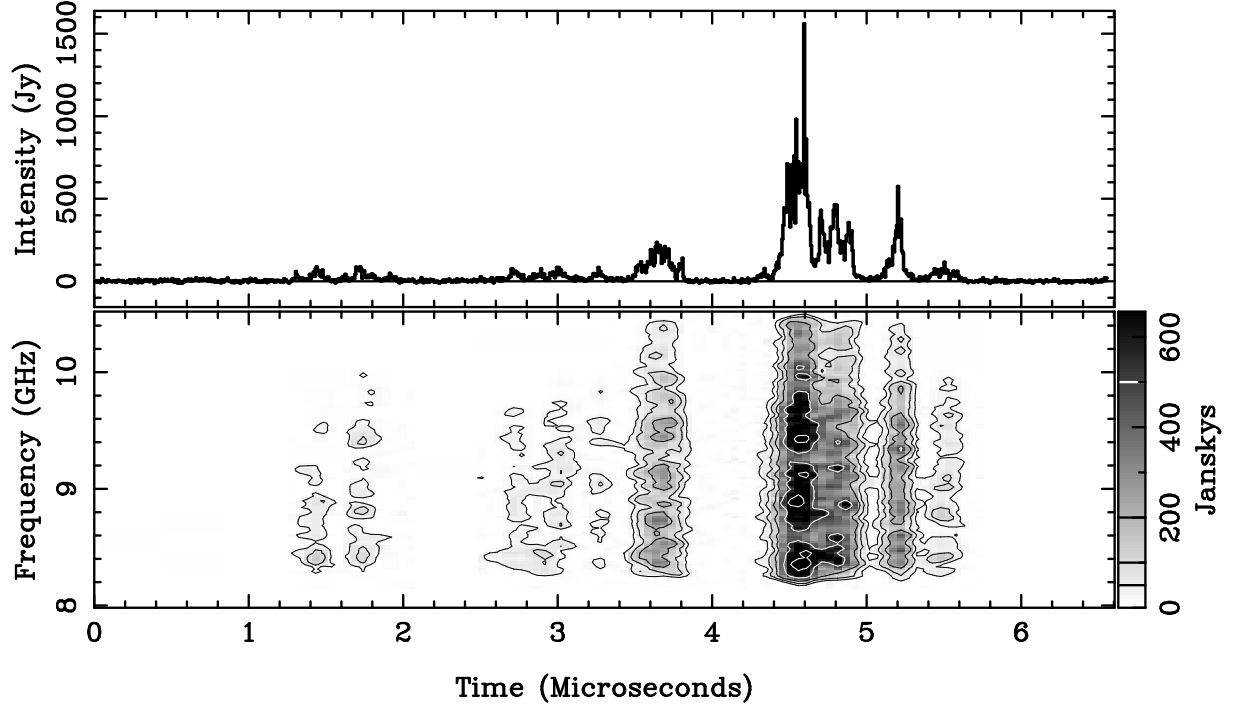


Fig. 2.— An example of a “normal” main pulse, processed with optimal dispersion measure, plotted with total intensity time resolution 6.4 ns, and dynamic spectrum resolution 51.2 ns, 19.5 MHz. The pulse seen in total intensity (upper panel) consists of several short-lived microbursts, which themselves contain shorter-duration nanoshots. The dynamic spectrum (lower panel) reveals that the microbursts are broad-band, spanning the 2.2-GHz receiver bandwidth. The lack of emission at the lower band edge is because the 2.5-GHz sampled bandwidth is slightly larger than the receiver passband; the high- ν fading is intrinsic to the star. The spectrum contour levels are 50, 100, 200, 500, and 1000 Jy.

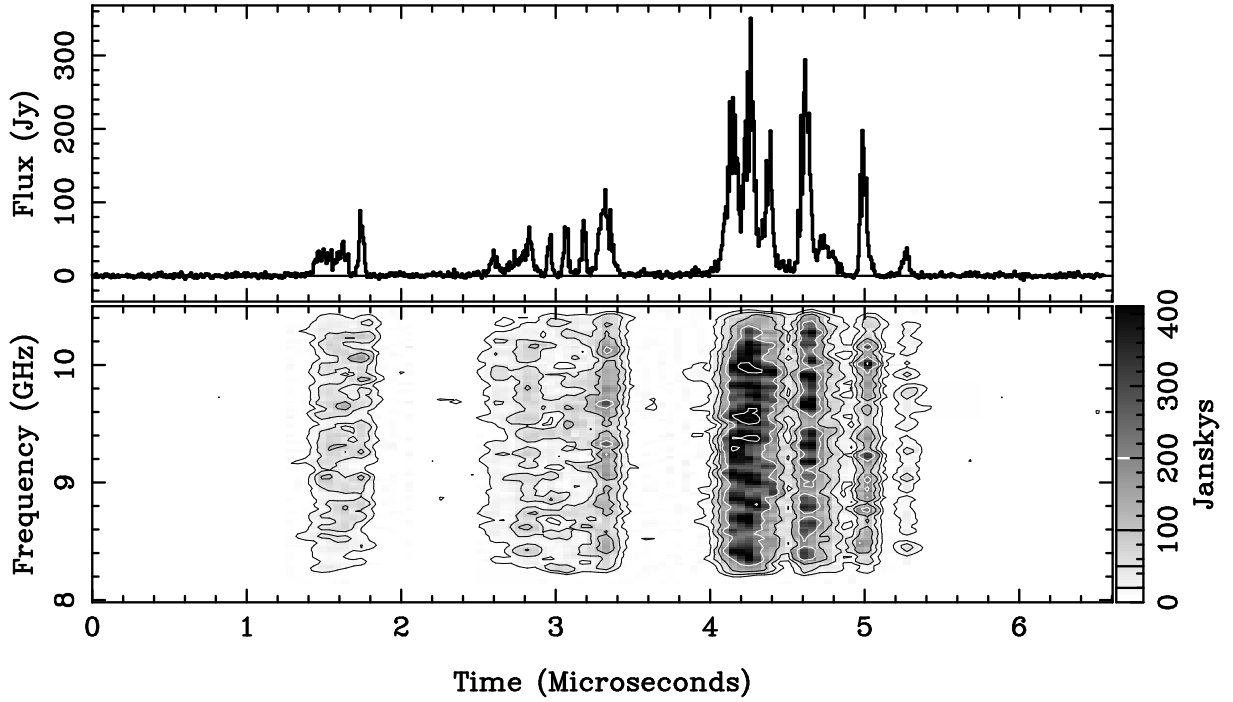


Fig. 3.— Another example of a “normal” main pulse, also processed with optimal dispersion measure. Similarly to the example in Figure 2, this pulse contains several short-lived microbursts, each of which contains shorter-duration nanoshots. This pulse differs from that in Figure 2 in that its dynamic spectrum does not fade to high frequencies. Total intensity time resolution 6.4 ns; dynamic spectrum resolution 51.2 ns, 19.5 MHz. Spectrum contour levels are 20, 50, 100, and 200 Jy.

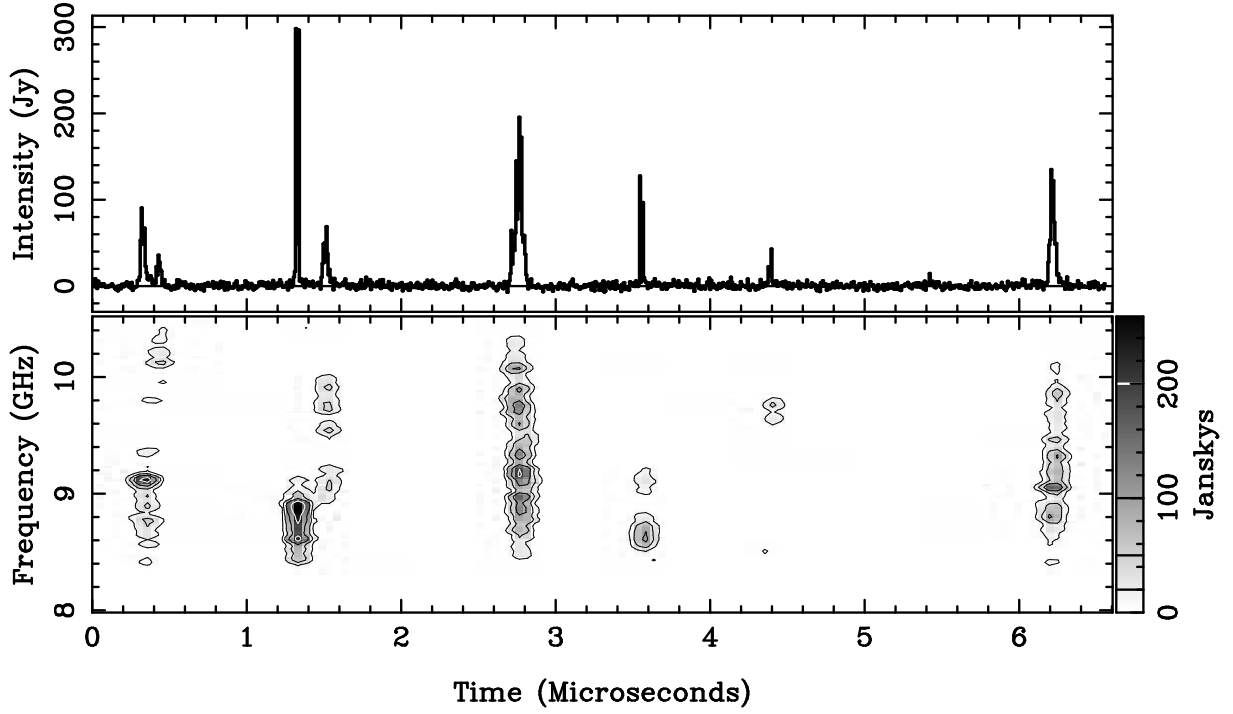


Fig. 4.— An example of a sparse main pulse at 9.25 GHz. The pulse is plotted with the same total intensity and dynamic spectrum resolution as the pulse in Figures 2 and 3. Occasionally nanobursts are sufficiently sparse that individual bursts with relatively narrow bandwidths can be identified, as seen here. The spectrum contour levels are 20, 50, 100, and 200 Jy.

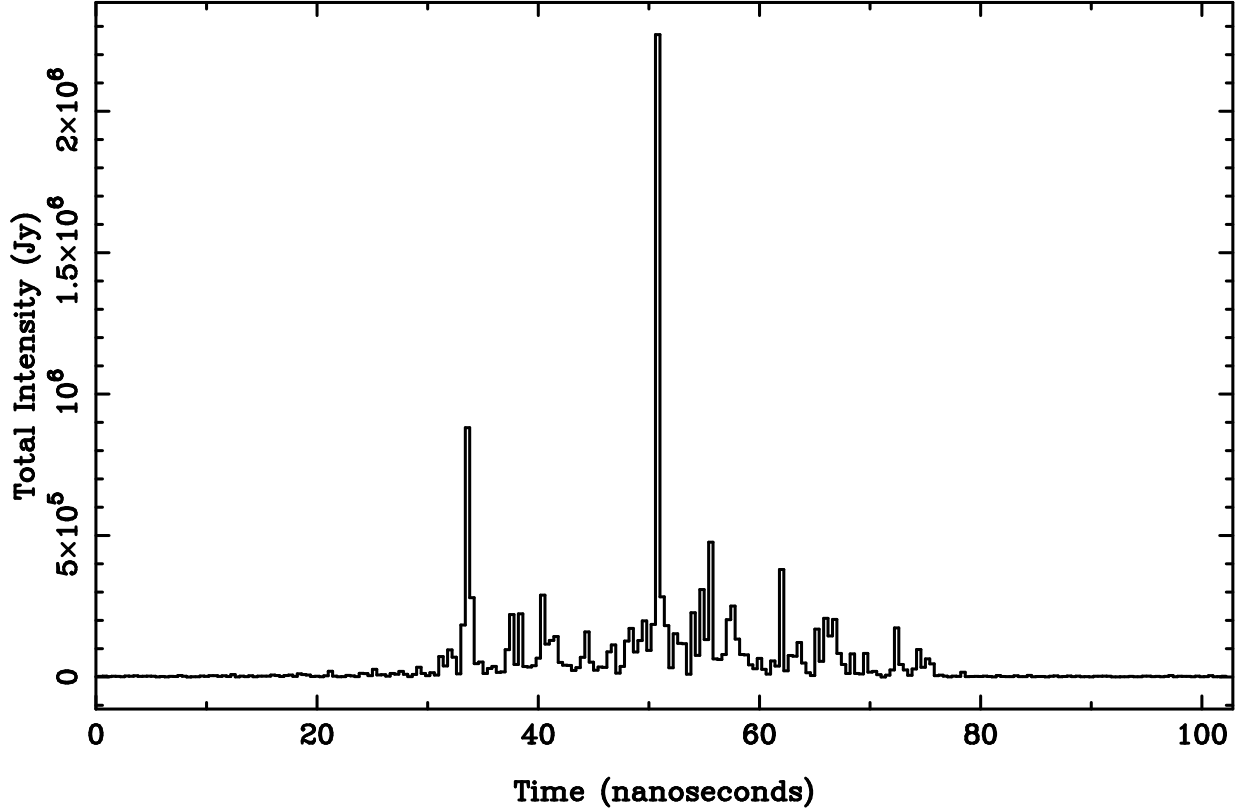


Fig. 5.— A single main pulse recorded at 9.25-GHz center frequency over a 2.2-GHz bandwidth and optimally dedispersed. The nanopulse shown is unresolved with the 0.4-ns time resolution afforded by our system. Despite the high peak intensity of this pulse, it is unlikely that it saturated the data acquisition system. The dispersion sweep time across the bandwidth is about 1.5 ms, so as sampled by our data acquisition system, the dispersed pulse energy is spread over $\approx 7.5 \times 10^6$ samples.

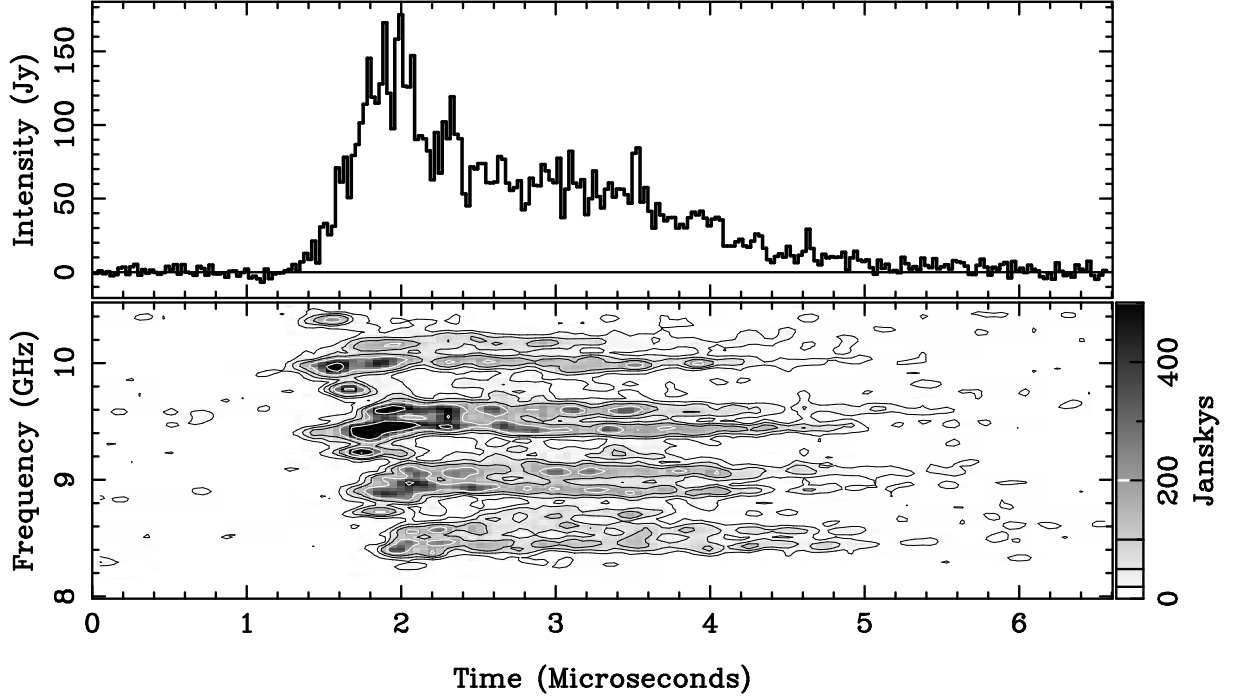


Fig. 6.— A typical interpulse, observed 12 minutes after the main pulse shown in Figure 2, and processed identically. The later arrival of bands at lower frequency implies that this pulse is more dispersed than the main pulse in Figure 2. The spectrum contour levels are 20, 50, 100, 200, 500 Jy. Total intensity time resolution is 51.2 ns; dynamic spectrum resolution is 51.2 ns, 19.5 MHz.

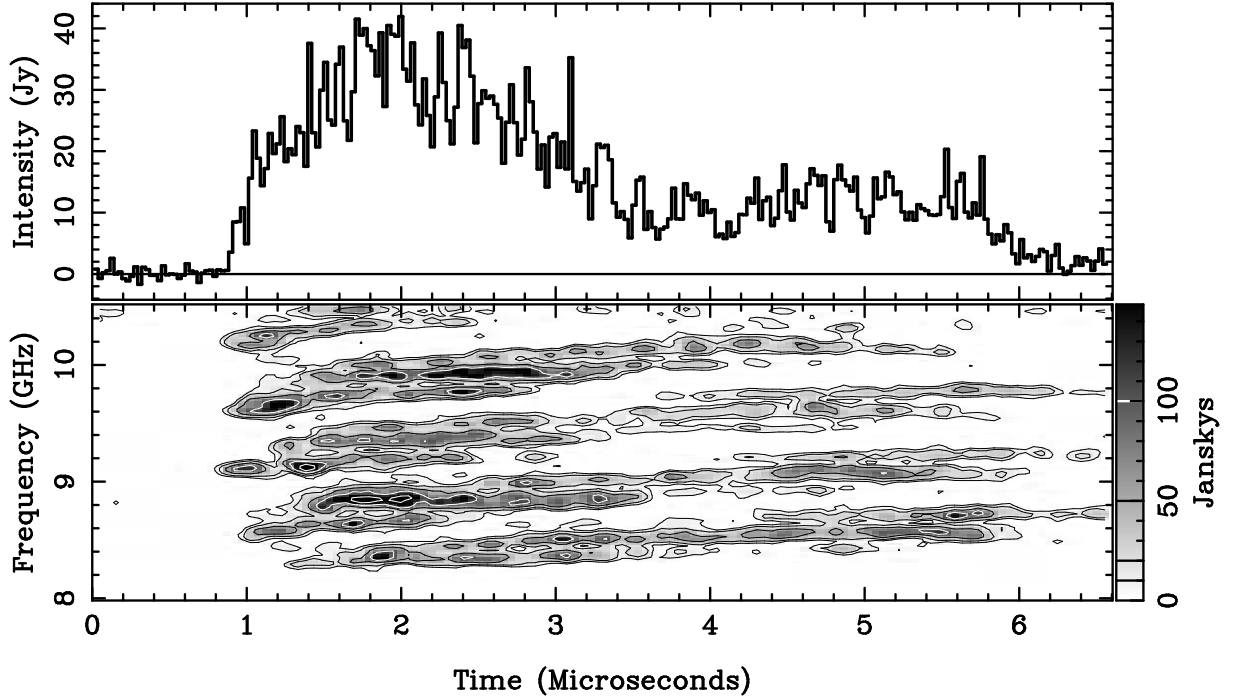


Fig. 7.— Another interpulse, processed with the “optimum” dispersion measure. All three of the pulses shown in Figures 6, 7 and 8 show the emission bands we discovered in the dynamic spectrum of the interpulse. As these examples show, several band sets can be identified within an interpulse. The interpulse usually starts with a short-lived band set, and continues with longer-lived sets, which either start at slightly higher frequencies or drift upwards in frequency. The onset of later band sets often coincides with a second burst in total intensity. As in Figures 2 and 3, the apparent lack of low- ν emission is because the sampled bandwidth is slightly larger than the receiver bandwidth. Unlike the main pulse in Figure 2, however, the band intensity does not fade toward high frequencies. Here and in Figure 8, the spectrum contour levels are 10, 20, 50, 100, 200 Jy. Total intensity time resolution is 51.2 ns; dynamic spectrum resolution is 51.2 ns, 19.5 MHz.

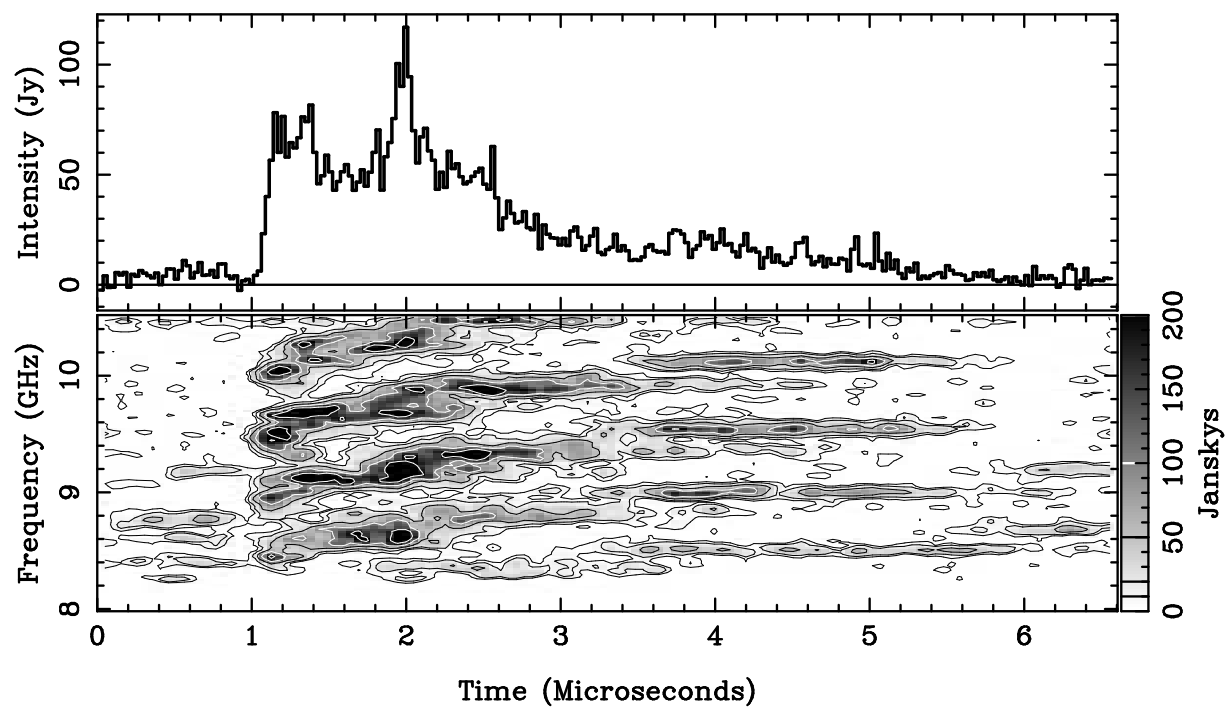


Fig. 8.— Another example of an interpulse, also processed with “optimum” DM and the same time and spectral resolution as in Figures 6 and 7.

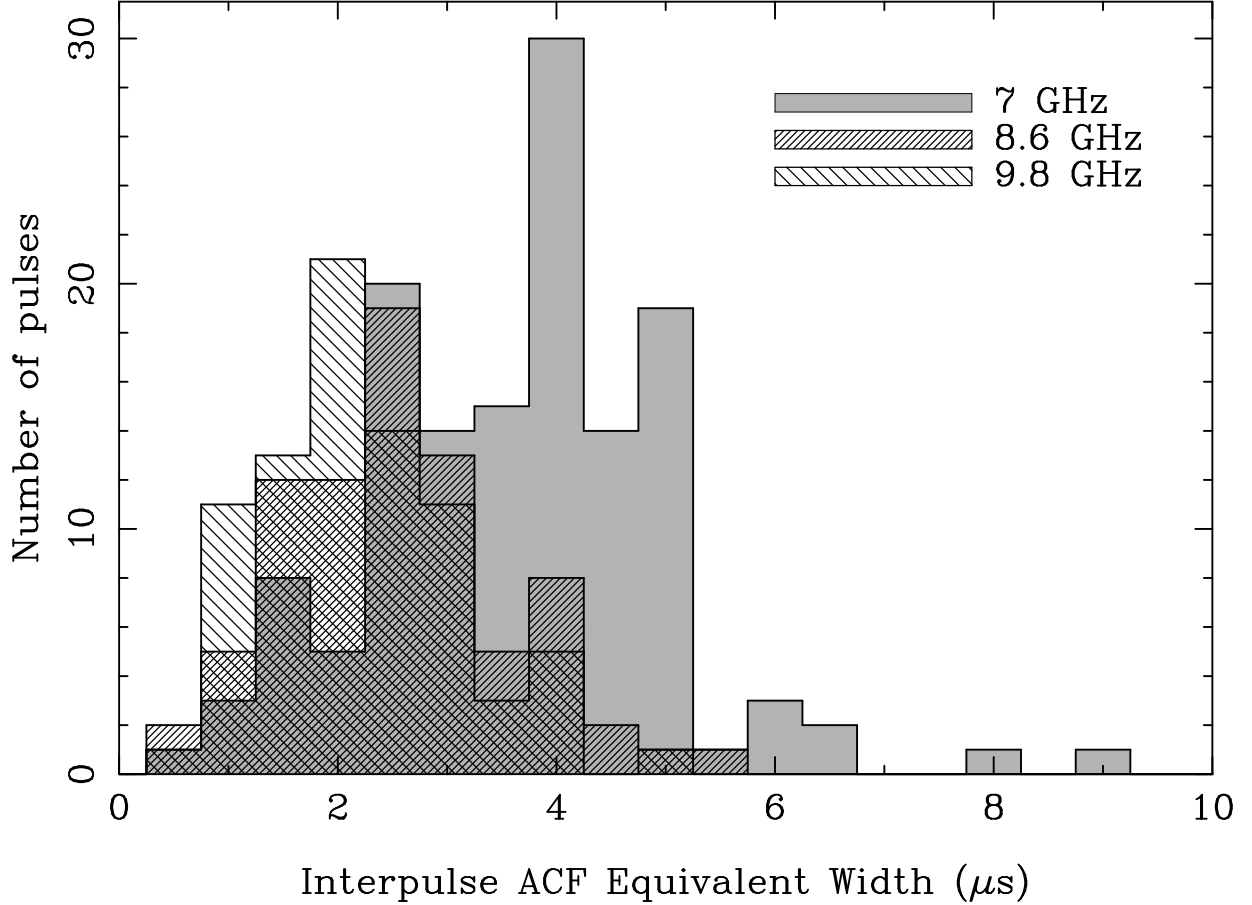


Fig. 9.— The distribution of time durations of our interpulses, as measured by the equivalent width of the autocorrelation function. Nearly all of the interpulses captured at frequencies between 6 and 8 GHz were recorded with a 1-GHz bandwidth; for these pulses we used the full bandwidth in computing the autocorrelation width. These pulses are labeled as 7 GHz in the figure. All of the interpulses between 8 and 10.5 GHz were recorded with a 2.5-GHz bandwidth. For these we divided the full band into high and low half-bands, each 1.25-GHz wide, centered at 8.625 and 9.875 GHz, and computed the autocorrelation width separately for each half-band. From the distribution of time durations it is clearly seen that the interpulse autocorrelation equivalent width is frequency dependent. The mean widths are 4.2, 3.0, and 2.7 μs for 7, 8.6 and 9.9 GHz, respectively.

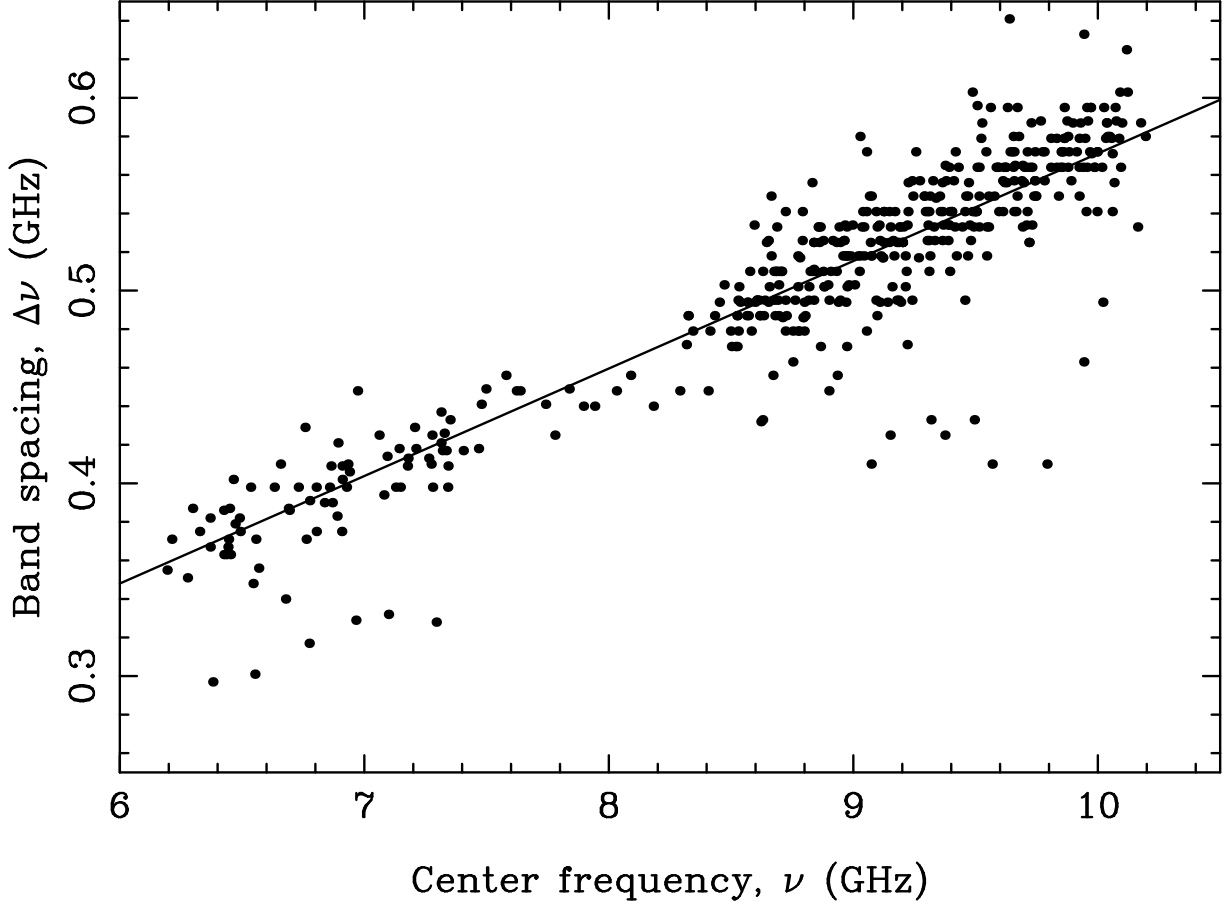


Fig. 10.— The emission band spacing, measured for 460 band sets in 105 pulses recorded on 20 observing days, is shown as a function of center frequency. The line is fitted to all of the points, and has the form $\Delta\nu = 0.058(\pm 0.001)\nu - 0.007(\pm 0.011)$.